CrossMark

J. Fluid Mech. (2017), *vol.* 812, *pp.* 1119–1145. © Cambridge University Press 2017
doi:10.1017/jfm.2016.800

Flow around an oscillating circular disk at low to moderate Reynolds numbers

Xinliang Tian[1,2], Longfei Xiao[1,2], Xiangdong Zhang[1,2], Jianmin Yang[1,2,†], Longbin Tao[3] and Dan Yang[4]

[1]State Key Laboratory of Ocean Engineering, Shanghai Jiao Tong University, Shanghai 200240, China

[2]Collaborative Innovation Center for Advanced Ship and Deep-Sea Exploration, Shanghai 200240, China

[3]School of Marine Science and Technology, Newcastle University, Newcastle upon Tyne NE1 7RU, UK

[4]School of Naval Architecture and Ocean Engineering, Huazhong University of Science and Technology, Wuhan 430074, China

(Received 25 February 2016; revised 21 November 2016; accepted 23 November 2016; first published online 12 January 2017)

Direct numerical simulations of the flow induced by a circular disk oscillating sinusoidally along its axis are performed. The aspect ratio (χ = diameter/thickness) of the disk is 10. The Reynolds number (Re), based on the maximum speed and the diameter of the disk, is in the range of $50 \leqslant Re \leqslant 800$. The Keulegan–Carpenter number (KC) is in the range of $1 \leqslant KC \leqslant 24$. Five flow regimes are observed in the considered Re–KC space: (I) axisymmetric flow (AS), (II) planar symmetric flow in the low-KC region (PSL), (III) azimuthally rotating flow in the low-KC region (ARL), (IV) planar symmetric flow in the high-KC region (PSH) and (V) azimuthally rotating flow in the high-KC region (ARH). The critical boundaries between different flow regimes are identified based on the evolutions of the magnitude and direction of transverse force acting on the disk. For the non-axisymmetric flow regimes, the flow is one-sided with respect to the axis of the disk and is associated with a non-zero mean value of the transverse force acting on the disk.

Key words: flow–structure interactions, vortex instability, vortex interactions

1. Introduction

Interest in the flow around a circular disk goes back many years. Many experimental studies (see, e.g. Marshall & Stanton 1931; Willmarth, Hawk & Harvey 1964; Kuo & Baldwin 1967; Roos & Willmarth 1971; Roberts 1973; Berger, Scholz & Schumm 1990; Fernandes *et al.* 2007; Zhong & Lee 2012) and numerical calculations (see, e.g. Michael 1966; Rimon 1969; Rivet *et al.* 1988; Fabre, Auguste & Magnaudet 2008; Shenoy & Kleinstreuer 2008; Auguste, Fabre & Magnaudet 2010; Chrust, Bouchet & Dušek 2010; Shenoy & Kleinstreuer 2010; Yang *et al.* 2014*a*, 2015) addressing this issue have been reported. As a typical case of an axisymmetric body, studies on circular disks are often conducted and discussed together with another typical

† Email address for correspondence: jmyang@sjtu.edu.cn

https://doi.org/10.1017/jfm.2016.800 Published online by Cambridge University Press

axisymmetric body, a sphere, which shares some similarities in the transition scenario (Fabre *et al.* 2008; Chrust *et al.* 2010).

The transition scenario in the wake of the uniform flow normal to a circular disk is dependent on both the Reynolds number and the aspect ratio of the disk. The aspect ratio of the disk is defined as $\chi = D/t_d$, where D and t_d are the diameter and thickness of the disk, respectively. A value of $\chi = \infty$ refers to an infinitely thin disk, which is sometimes called a 'flat disk' in the literature. It has been reported that the flow is steady and axisymmetric at sufficiently low Reynolds numbers, corresponding to the 'trivial state' (TS), as it has been named by Auguste *et al.* (2010). The first bifurcation occurs at the critical value of the Reynolds number, Re_{c1}, resulting in a reflectionally symmetric flow represented by a pair of steady streamwise vortices and a steady lift force. This state has been named a 'steady state' (SS) by Fabre *et al.* (2008) and Meliga, Chomaz & Sipp (2009) and a 'steady asymmetric state' by Shenoy & Kleinstreuer (2008). According to direct numerical simulation (DNS) results for disks with $\chi = 2, 3, 4, 6$ and 10, the relation between the critical Reynolds number and the aspect ratio of the disk can be described as $Re_{c1} \approx 116.5(1 + \chi^{-1})$ (Fernandes *et al.* 2007). For a flat disk ($\chi = \infty$), a reasonable consensus that the value of Re_{c1} is between 115 and 117 has been achieved (Natarajan & Acrivos 1993; Fabre *et al.* 2008; Meliga *et al.* 2009; Chrust *et al.* 2010). For a disk of $\chi = 10$, Re_{c1} has been reported to be 135 by Shenoy & Kleinstreuer (2008) and 129.6 by Chrust *et al.* (2010). A value of $Re_{c1} \approx 159.4$ has been reported by Auguste *et al.* (2010) for a thicker disk with $\chi = 3$.

A secondary Hopf bifurcation occurs as the Reynolds number increases further. The new state is characterized as a 'three-dimensional periodic flow with regular rotation' (Shenoy & Kleinstreuer 2008). Unlike in the case of the sphere, the lift force of the disk in this state is azimuthally oscillating. This state has also been referred to as a 'Yin-Yang' (YY) state by Auguste *et al.* (2010), a 'mixed mode with phase π' (MM_π) by Meliga *et al.* (2009) and 'reflectional symmetry breaking' (RSB) by Fabre *et al.* (2008). The critical Reynolds number for the secondary bifurcation (Re_{c2}) has been reported to lie between 121 and 125.6 for a flat disk ($\chi = \infty$) (Natarajan & Acrivos 1993; Fabre *et al.* 2008; Chrust *et al.* 2010) and between 136.3 and 138.7 (Chrust *et al.* 2010) or at approximately 155 (Shenoy & Kleinstreuer 2008) for a disk with $\chi = 10$.

As the Reynolds number increases still further, depending on the aspect ratio of the disk, the transition scenarios and the critical Reynolds numbers between different flow states become more complicated. Auguste *et al.* (2010) investigated the bifurcations in the wake of a disk with $\chi = 3$. It was reported that at least four additional bifurcations are encountered before a chaotic state is reached, namely, the 'Zig–zig' (Zz), 'Knit-Knot' (KK), 'Yin–Yang' (YY) and 'Zig–Zag' (ZZ) modes. Chrust *et al.* (2010) conducted an extensive parametric study of the transition scenario in the wake of a disk with $\chi \geqslant 1$. A very detailed and systematic picture of the transition scenario was presented in the two-parameter space of the Reynolds number and the aspect ratio of the disk. A more detailed review is provided by Ern *et al.* (2012).

Apart from the studies of the flow around a fixed disk, the instabilities in the wake and path of a freely falling (or rising) disk under the action of gravity (or buoyancy) have attracted extensive attention. According to the experimental studies performed by Zhong & Lee (2012), the wake transition scenarios are similar to those of the flow patterns behind a fixed disk. The transition from axisymmetry to plane symmetry was found at $Re_{c1} \approx 105$, while the Hopf bifurcation occurred at $Re_{c2} \approx 118$. Although such investigations on the first bifurcations in the wake of a fixed disk have indeed

https://doi.org/10.1017/jfm.2016.800 Published online by Cambridge University Press

furthered the understanding of the mechanisms of the oscillatory motion of the freely moving disk, there is no doubt that the latter case is significantly more complicated. The problem of freely falling or rising bodies in a fluid at rest is governed by three control parameters: the geometrical parameter χ, the body-to-fluid density ratio $\bar{\rho}$ and the Archimedes number Ar. One of the widely accepted propositions is that the presence of vorticity in the flow is the only source of path instability. However, this does not mean that the dynamics of the freely moving disk can be considered as that of a fixed disk. Fernandes *et al.* (2007) reported a delayed onset of instabilities for a freely rising disk compared with that of a fixed disk. This finding was later confirmed by Chrust, Bouchet & Dušek (2014). In other words, the freedom of the disk has a stabilizing effect on the onset of the primary bifurcation. Moreover, Auguste, Magnaudet & Fabre (2013) noted that it was essentially incorrect to expect that the bifurcations for the falling body to closely mirror the wake of the same disk held fixed in a uniform stream. The dynamics of the wake and path of a freely moving disk are intrinsically coupled. Therefore, the stability analysis of this type of problem must consider the body + fluid system as fully coupled (Tchoufag, Fabre & Magnaudet 2014).

Undoubtedly significant insight into the fluid dynamics of a disk has been achieved through these numerous experimental and numerical simulations. Nevertheless, there are still some aspects that are not fully understood and merit further investigation. With regard to the flow configurations, the steady flow over a fixed circular disk or a freely falling/rising circular disk in a stationary fluid were considered in the previous studies. In both of these cases, the flow relative to the disk is only in one direction, and the wake flow is always behind the disk. By contrast, the oscillatory flow over a circular cylinder or a circular cylinder oscillating in a quiescent fluid has been extensively studied (see, e.g. Bearman 1984; Williamson & Govardhan 2008; An, Cheng & Zhao 2011). Unfortunately, to the best of our knowledge, similar studies have not yet been performed for the circular disk. For a disk oscillating in a fluid at rest, the disk moves back and forth, accelerates and decelerates. Some new and interesting phenomena are expected to be revealed. This is the motivation of the present study, and four questions are to be answered: (i) what is the wake of the oscillating disk, (ii) how many types of flow regimes exist, (iii) what is the dependence of the threshold on the oscillating amplitude and Reynolds number and (iv) what is the connection between the wake instabilities of a fixed disk and those of an oscillating disk.

With these questions, we start our study by considering the simplest case: an isolated circular disk that is forced to oscillate sinusoidally along its axis. Here, we introduce the coordinate system (x, y, z), whose origin is located at the centre of the disk. The z-axis of the coordinate system is parallel with the axis of the disk. The axial displacement of the disk is a function of time: $z_{disk}(t) = a\sin(2\pi t/T)$, where a is the amplitude of the oscillatory motion, T is the period of oscillation and t is the time. Therefore, the axial velocity of the disk is taken as $u_z(t) = U_{max}\cos(2\pi t/T)$, where U_{max} is the maximum speed of the disk, i.e. $U_{max} = 2\pi a/T$.

It has been reported that the aspect ratio of the disk plays a significant role in determining the transition process and vortex structure in the wake of a steady flow (Shenoy & Kleinstreuer 2010). Therefore, the key dimensionless parameters that define the problem are the Reynolds number (Re), the Keulegan–Carpenter number (KC) and the disk aspect ratio χ. The respective definitions of Re and KC are given as follows:

$$Re = \frac{U_{max}D}{\nu}, \tag{1.1}$$

https://doi.org/10.1017/jfm.2016.800 Published online by Cambridge University Press

$$KC = \frac{U_{max}T}{D} = \frac{2\pi a}{D}, \tag{1.2}$$

where ν is the kinematic viscosity of the fluid.

It is noteworthy that, according to the study for the transition scenario in the wake of a fixed disk by Chrust *et al.* (2015), the supporting structure is one of the main sources resulting in the discrepancies between the numerical and experimental results. The flow regimes in the present oscillating case may also be influenced by the supporting structure. In the present study, we attempted to reveal the fundamental fluid dynamics of an oscillating circular disk. Therefore, the supporting structure is not considered. In this case, numerical method is a more appropriate technique because the very ideal conditions could be achieved easily in numerical simulations.

The DNS method was used to calculate the flow around the disk, and the deforming mesh technique was employed to simulate the oscillatory motion of the disk. The ranges of Re and KC considered in the present study are $50 \leqslant Re \leqslant 800$ and $1 \leqslant KC \leqslant 24$, respectively. The disk aspect ratio considered in this study is 10, which can be reasonably regarded as representative of a 'thin' disk (Chrust *et al.* 2010). Another reason for the selection of an aspect ratio of 10 is for convenience in comparing the obtained results with the DNS results reported by Shenoy & Kleinstreuer (2008).

The remainder of this paper is organized as follows. Details of the numerical simulations are presented in § 2. The results are described in § 3. Finally, a few concluding remarks are offered in § 4.

2. Numerical simulations

2.1. *Mathematical formulations and numerical methods*

We consider a rigid circular disk that is forced to oscillate along its axis in a Newtonian incompressible fluid at rest. The Cartesian coordinate system (x, y, z) is used in the present study. If these coordinates are labelled as (x_1, x_2, x_3) and the velocity component in the x_i direction is denoted by u_i, where $i = 1$–3, then the Navier–Stokes (N–S) equations can be expressed as follows:

$$\frac{\partial u_i}{\partial x_i} = 0, \tag{2.1}$$

$$\frac{\partial u_i}{\partial t} + u_j \frac{\partial u_i}{\partial x_j} = -\frac{1}{\rho}\frac{\partial p}{\partial x_i} + \nu \frac{\partial^2 u_i}{\partial x_j \partial x_j}, \tag{2.2}$$

where p is the pressure and ρ is the density of the fluid. For clarity, the velocity components u_1, u_2 and u_3 are also denoted by u_x, u_y and u_z, respectively.

The N–S equations are discretized using the finite volume method (FVM) based on the open-source computational fluid dynamics (CFD) code *OpenFOAM*. *OpenFOAM* is primarily applied for solving problems in continuum mechanics. It is built based on the tensorial approach and object-oriented techniques (Weller *et al.* 1998). The pressure-implicit with splitting of operators (PISO) scheme (*pisoFoam*) is used in the present study. The spatial schemes used for interpolation, gradient, Laplacian and divergence calculations are the linear, Gauss linear, Gauss linear corrected and Gauss linear schemes, respectively. All these schemes were of second order. The second-order Crank–Nicholson scheme was used for the time integration. Further details of these schemes are provided in OpenFOAM (2009).

https://doi.org/10.1017/jfm.2016.800 Published online by Cambridge University Press

The non-dimensional force coefficients in three directions, i.e. the x, y and z directions, are defined as follows:

$$(C_x, C_y, C_z) = \frac{(F_x, F_y, F_z)}{\frac{1}{8}\rho U_{ref}^2 \pi D^2}, \tag{2.3}$$

where F_x, F_y and F_z are the force components acting on the disk in the x, y and z directions, respectively, and they are directly calculated by integrating the pressure and viscous shear stress over the disk surface; in the case of the analysis of the steady flow over a fixed disk performed for code validation (see § 2.2), the reference speed (U_{ref}) is the free stream speed (U_s), and in the case of the oscillating disk, U_{ref} is the maximum speed of the disk (U_{max}).

The so-called Q-criterion proposed by Hunt, Wray & Moin (1988) and the vorticity component in the z direction (ω_z) are used to identify the vortical structures around the disk. Q is defined as

$$Q = -\tfrac{1}{2}(\|\boldsymbol{S}\|^2 - \|\boldsymbol{\Omega}\|^2), \tag{2.4}$$

where $\boldsymbol{S}$ and $\boldsymbol{\Omega}$ denote the strain and the rotation tensor, respectively.

2.2. *Code validation*

To validate the adopted numerical approach, benchmark calculations of the steady flow normal to a stationary disk are performed. Following the set-up presented by Shenoy & Kleinstreuer (2008), the aspect ratio of the disk is $\chi = 10$. A cylindrical computational domain with a cross-sectional diameter l_r is used; see figure 1(*a*). The origin of the coordinate system (x, y, z) is located at the centre of the disk, and the z-axis coincides with the axis of the disk. The distances from the inlet and outlet boundaries to the centre of the disk are denoted as l_u and l_d, respectively. On the disk surface, no-slip and zero normal-pressure-gradient boundary conditions are imposed. At the inlet boundary, a uniform velocity $(0, 0, U_s)$ and zero normal-pressure-gradient boundary conditions are prescribed. At the outlet boundary, the velocity is set to a zero normal gradient and the pressure is fixed at zero. At the free stream boundary, free-slip and zero normal-gradient boundary conditions are applied for the velocity and pressure, respectively. The topology of the mesh also follows that used in Shenoy & Kleinstreuer (2008), and the computational domain is discretized with hexahedral elements; see figure 1(*b*). In the vicinity of the disk, the grids are finer to better resolve the steep gradient in this region. To assess the effects of the spatial and temporal resolutions on the results, three cases with different spatial and temporal resolutions are considered; see cases S1–S3 in table 1, where n_1 denotes the element size in the wall-normal direction near the disk surface, Δt is the time step used in the simulations, Re_s denotes the Reynolds number based on the free stream velocity (U_s) and the disk diameter (D) and L_w denotes the recirculation length, which is defined as the streamwise distance from the centre of the disk to the position where the streamwise velocity changes sign from negative to positive. In the considered Reynolds number region (i.e. $Re_s < Re_{c1}$), the flow is steady and axisymmetric (Auguste *et al.* 2010). As shown in table 1, only very small variations are observed in the results for C_z and L_w calculated for the different spatial and temporal resolutions, i.e. for cases S1–S3. To further assess the effects of the size of the computational domain on the calculated results, two more cases are conducted with a reduced computational domain size, see cases S4 and S5 in table 1. The

https://doi.org/10.1017/jfm.2016.800 Published online by Cambridge University Press

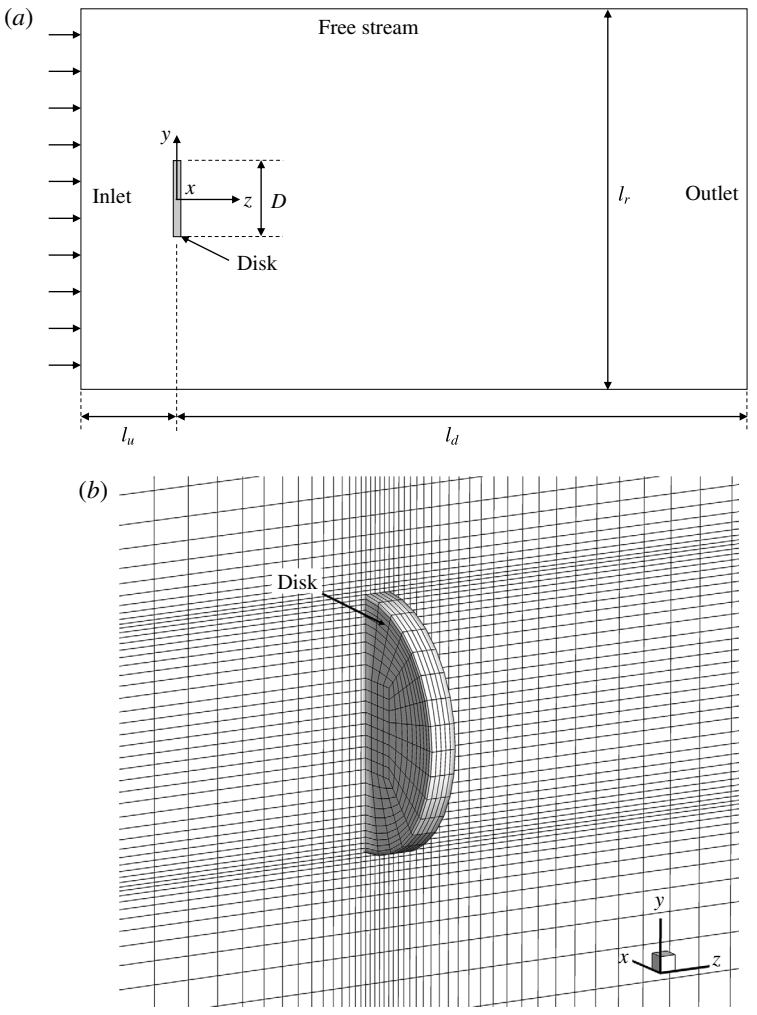


FIGURE 1. Stationary disk: (*a*) computational domain and boundary conditions (not to scale) and (*b*) grid structures near the disk surface.

meshes used in cases S3–S5 are designed to be of an equivalent density. As shown in table 1, a good convergence is observed in the results of C_z and L_w for cases S3–S5. It is concluded that the effects of the size of the computational domain on the calculated results are negligible for case S3. Finally, the axial drag coefficient (C_z) and recirculation length (L_w) obtained for case S3 are in good agreement with the DNS results reported by Shenoy & Kleinstreuer (2008) and the experimental measurements reported by Roos & Willmarth (1971); see figure 2.

To validate the capability of the present numerical approach for computing the unsteady wake flow, numerical simulations are conducted for Reynolds numbers of $Re_s = 160$ and 180. As shown in table 2, the Strouhal number St represents the wake frequency non-dimensionalized with the free stream velocity (U_s) and the diameter of the disk (D). Similar to the validation studies for the steady cases shown in table 1, the effects of the grid resolution, time step and computational domain size are also evaluated. The configurations of cases S1–S5 are kept the same as those shown in

https://doi.org/10.1017/jfm.2016.800 Published online by Cambridge University Press

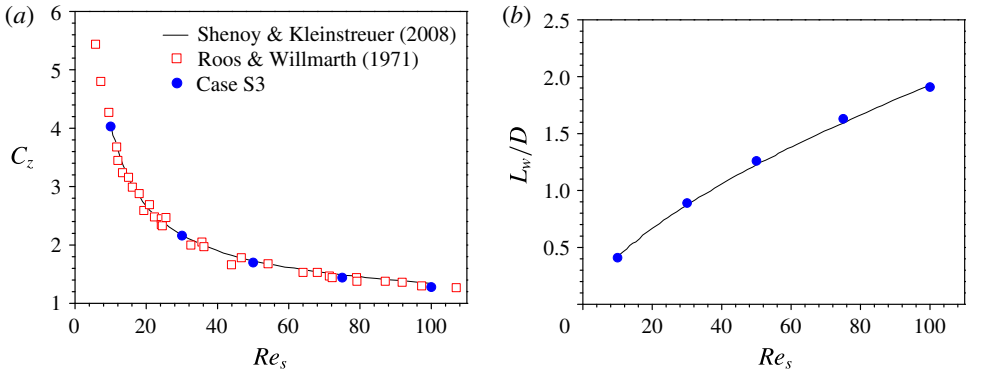


FIGURE 2. (Colour online) Comparisons of the results for the steady flow normal to a circular disk: (*a*) axial drag coefficient (C_z) and (*b*) recirculation length (L_w).

						Domain size			Re_s				
	Case	Elements		n_1/D	$\Delta tU_s/D$	l_u/D	l_d/D	l_r/D	10	30	50	75	100
C_z	S1	107	520	0.02	0.01	5	30	24	4.00	2.15	1.70	1.43	1.28
	S2	365	184	0.0133	0.0075	5	30	24	4.02	2.16	1.71	1.44	1.28
	S3	860	160	0.01	0.005	5	30	24	4.03	2.16	1.70	1.44	1.28
	S4	735	360	0.01	0.005	4	24	18	4.06	2.18	1.72	1.45	1.29
	S5	599	040	0.01	0.005	2.5	15	12	4.21	2.25	1.78	1.50	1.34
L_w/D	S1	107	520	0.02	0.01	5	30	24	0.40	0.87	1.24	1.60	1.88
	S2	365	184	0.0133	0.0075	5	30	24	0.40	0.88	1.25	1.62	1.90
	S3	860	160	0.01	0.005	5	30	24	0.41	0.89	1.26	1.63	1.91
	S4	735	360	0.01	0.005	4	24	18	0.41	0.89	1.26	1.63	1.91
	S5	599	040	0.01	0.005	2.5	15	12	0.41	0.90	1.27	1.64	1.93

TABLE 1. Results for the axial drag coefficient (C_z) and the recirculation length (L_w) obtained for cases of different configurations for a stationary disk. The values of C_z and L_w/D are shown in the last five columns.

table 1. It is observed that the results of *St* in the present converged case S3 agree well with the results obtained in the literature (Shenoy & Kleinstreuer 2008; Chrust *et al.* 2010; Yang *et al.* 2014*c*).

Overall, the present numerical approach yields reliable results for the flow over a circular disk. Moreover, this numerical approach has previously been successfully applied to calculate the incompressible flow around an oscillating disk (Yang, Tian & Li 2014*b*).

2.3. *Computational domain and boundary conditions*

A spherical computational domain of radius R_{domain} is used for the oscillating disk; see figure 3(*a*). The origin of the coordinate system is located at the centre of the computational domain, and the *z*-axis coincides with the axis of the disk. The mean position of the disk is at the centre of the computational domain. On the disk surface, the no-slip boundary condition is imposed for the velocity; the pressure is set to a zero normal gradient. At the outer boundary, the velocity is set to a zero normal gradient

https://doi.org/10.1017/jfm.2016.800 Published online by Cambridge University Press

Case	χ	Re_s	St
Present (S1)	10	160	0.118
Present (S2)	10	160	0.115
Present (S3)	10	160	0.114
Present (S4)	10	160	0.115
Present (S5)	10	160	0.120
Present (S1)	10	180	0.120
Present (S2)	10	180	0.117
Present (S3)	10	180	0.116
Present (S4)	10	180	0.116
Present (S5)	10	180	0.122
Shenoy & Kleinstreuer (2008)	10	160	0.113
Shenoy & Kleinstreuer (2008)	10	180	0.113
Chrust *et al.* (2010)	10	(136.3,138.7)	0.115
Chrust *et al.* (2010)	10	154.4	0.114
Yang *et al.* (2014*c*)	5	152	0.113
Yang *et al.* (2014*c*)	5	172	0.113

TABLE 2. Comparisons of the Strouhal number for a stationary disk obtained in different studies.

and the pressure is fixed at zero. It has been checked carefully that the effects of the boundary condition at the outer boundary on the calculated results are negligible in the present configuration. The entire computational domain is discretized with hexahedral elements, and the grid near the disk surface is of finer resolution to resolve the steep gradient in this region; see figure 3.

The oscillatory motion of the disk is realized using the deforming mesh method, in which the topology of the mesh does not change throughout the simulation. The mesh is updated at each time step by moving the grid points based on the permanent static mesh with $z_{disk} = 0$, which is established at the beginning of the simulation (see figure 3*a* as an example). To preserve the validity and quality of the mesh, a grid-smoothing method is applied, which is described as follows. Let $\boldsymbol{r}^i(t)$ represent the coordinates of point i at time t, and let $\boldsymbol{r}_{disk}(t) = (0, 0, z_{disk})$ represent the displacement of the disk at time t; then, $\boldsymbol{r}^i(t)$ can be determined using the following equation:

$$\boldsymbol{r}^i(t) = \boldsymbol{r}^i(0) + \boldsymbol{r}_{disk}(t) f^*. \tag{2.5}$$

The scaling function f^* in equation (2.5) is determined by the distance of the grid point from the centre of the disk as follows:

$$f^* = \begin{cases} 1 & \text{if } |\boldsymbol{r}^i(0)| \leqslant R_1 \\ 0.5 \sin\left[\pi\left(\dfrac{|\boldsymbol{r}^i(0)| - R_2}{R_1 - R_2} - 0.5\right)\right] + 0.5 & \text{if } R_1 < |\boldsymbol{r}^i(0)| < R_2 \\ 0 & \text{if } |\boldsymbol{r}^i(0)| \geqslant R_2. \end{cases} \tag{2.6}$$

Here, the values of R_1 and R_2 in equation (2.6) are taken to be $R_1 = 2.5D$ and $R_2 = R_{domain}$, respectively, where R_{domain} is the radius of the spherical computational domain. Using the scaling function f^*, a smooth grid deformation can be obtained between the disk and the outer boundary. Thus, a good mesh quality can always be maintained during a simulation. Figure 3(*b*) shows an example of the grid structures at the maximum amplitude considered in this study, i.e. $z_{disk} = 3.82D$ at $KC = 24$.

https://doi.org/10.1017/jfm.2016.800 Published online by Cambridge University Press

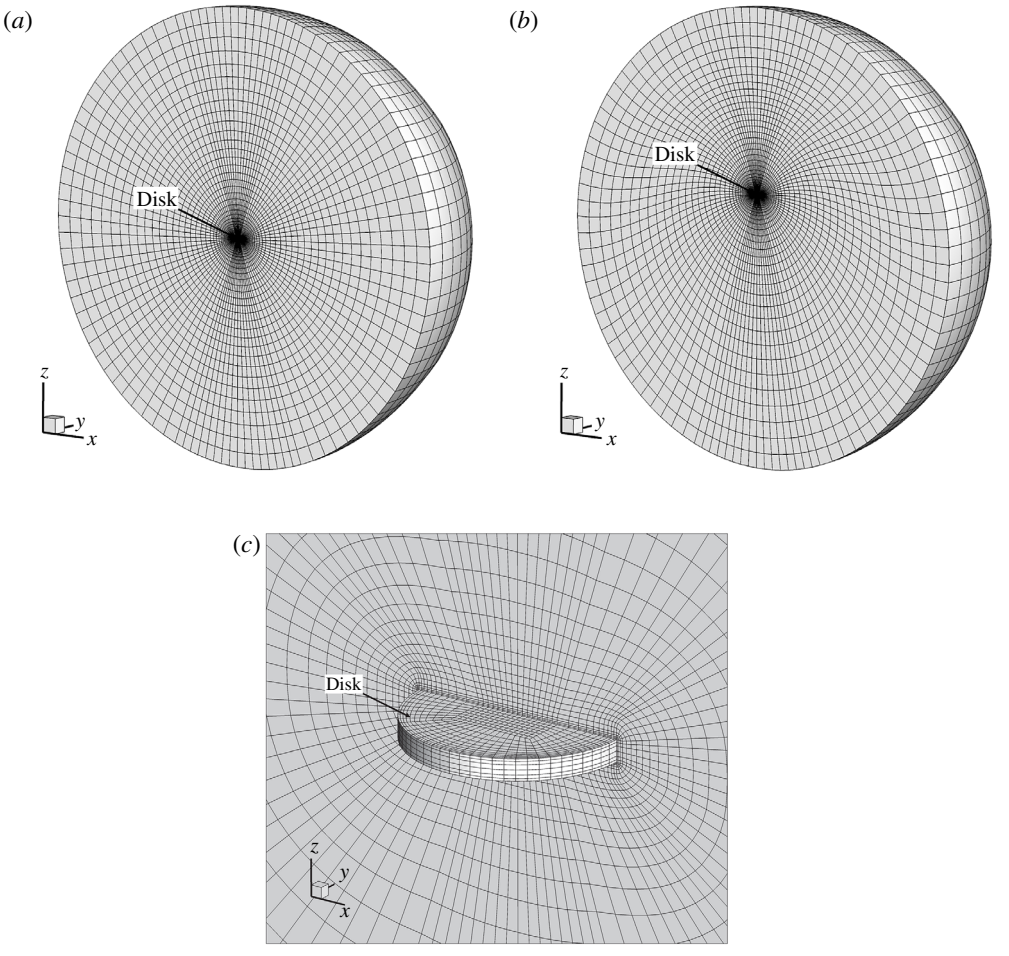


FIGURE 3. Oscillating disk: cut-away views of the computational domain and grid structures (*a*) at the mean disk position $z_{disk} = 0$, (*b*) at the maximum disk displacement ($z_{disk} \approx 3.82D$ at $KC = 24$ as an example) and (*c*) in a detailed zoom of the region near the disk surface.

2.4. *Convergence studies*

To assess the effects of the spatial and temporal resolutions on the calculated results, three cases with different numbers of grid elements and time steps, i.e. cases *O*1–*O*3 in table 3, are considered. For each case, the results for three different flow configurations, i.e. $(Re, KC) = (245, 24.5)$, $(600, 15)$ and $(900, 7.5)$, are presented. The parameters C_D and C_M shown in table 3 are the drag and inertia coefficients, respectively, which are calculated by splitting the axial force (F_z) into drag and inertial terms following the Morison equation (Morison *et al.* 1950), which states that

$$F_z = -C_D \rho \frac{\pi}{8} D^2 u_z(t)|u_z(t)| - C_M \rho \frac{\pi}{4} t_d D^2 \dot{u}_z(t). \tag{2.7}$$

In this study, C_D and C_M were calculated using the least-squares method. As shown in table 3, for all three considered flow configurations, the results of C_D and C_M obtained in cases *O*2 and *O*3 agree well with each other, indicating reasonable

https://doi.org/10.1017/jfm.2016.800 Published online by Cambridge University Press

Case	Elements		n_1/D	R_{domain}	$T/\Delta t$	$Re = 245$ $KC = 24.5$		$Re = 600$ $KC = 15$		$Re = 900$ $KC = 7.5$	
						C_D	C_M	C_D	C_M	C_D	C_M
$O1$	117	760	0.0055	$20D$	5 000	1.48	14.82	1.51	14.07	1.84	11.13
$O2$	397	440	0.0036	$20D$	10 000	1.42	17.15	1.44	14.07	1.78	11.08
$O3$	942	080	0.0027	$20D$	15 000	1.42	17.15	1.44	13.83	1.76	11.23
$O4$	457	920	0.0036	$30D$	10 000	1.43	17.00	1.46	13.87	1.78	11.11

TABLE 3. Results for the drag coefficient (C_D) and inertia coefficient (C_M) obtained for cases of different spatial and temporal resolutions for an oscillating disk.

convergence with increasing spatial and temporal resolutions. The effects of the size of the computational domain on the calculated results are evaluated by considering a larger domain of radius $R_{domain} = 30D$; see case $O4$ in table 3. Case $O4$ corresponds to a similar spatial resolution and the same time step in case $O2$. The results for C_D and C_M obtained in case $O4$ agree well with those in cases $O2$ and $O3$, indicating that a computational domain of radius $R_{domain} = 20D$ is sufficient to eliminate the effects of the outer boundary on the calculated results.

Moreover, the time traces of C_z for the three considered (Re, KC) configurations are plotted against z_{disk} in figure 4. Good consistency is found among the results of cases $O2$–$O4$; this again demonstrates that the effects of the spatial and temporal resolutions and of the size of the computational domain on the calculated results are negligible in the present study. In the following, all reported simulations are performed using the set-up used in case $O2$, i.e. with 397 440 grid elements, a time step of $T/10000$ and a computational domain of radius $20D$.

3. Results and discussion

According to the DNS studies performed by Shenoy & Kleinstreuer (2008) concerning the uniform flow normal to a circular disk of $\chi = 10$, the flow is steady and axisymmetric about the axis of the disk when $Re < 135$. As the Reynolds number increases, regular bifurcation with a loss of azimuthal symmetry occurs. Similarly, for the oscillating disk considered in the present study, non-axisymmetric bifurcation may occur as Re and KC vary. Here, the flow regimes around a circular disk of $\chi = 10$ are investigated in the considered Re–KC space, i.e. for $50 \leqslant Re \leqslant 800$ and $1 \leqslant KC \leqslant 24$.

Numerical simulations were performed for 151 pairs of Re and KC values represented by solid dots in figure 5. Preliminary inspection on the calculated flow field indicates that there are at least three types of flow regimes in the considered Re–KC space, i.e., one axisymmetric flow region in the middle and two non-axisymmetric flow regions in the low- and high-KC regions. It is noteworthy that the onset of non-axisymmetry is not always clear cut. The magnitude of the transverse force acting on the disk is closely related to the level of non-axisymmetry of the flow. Here, the magnitude of the transverse force coefficient is calculated as $C_{xy} = \sqrt{C_x^2 + C_y^2}$. Close to the threshold of the axisymmetric and non-axisymmetric regimes, any perturbation is either exponentially amplified or damped. Therefore, the accurate threshold is determined by linear interpolation of the growth rate of

https://doi.org/10.1017/jfm.2016.800 Published online by Cambridge University Press

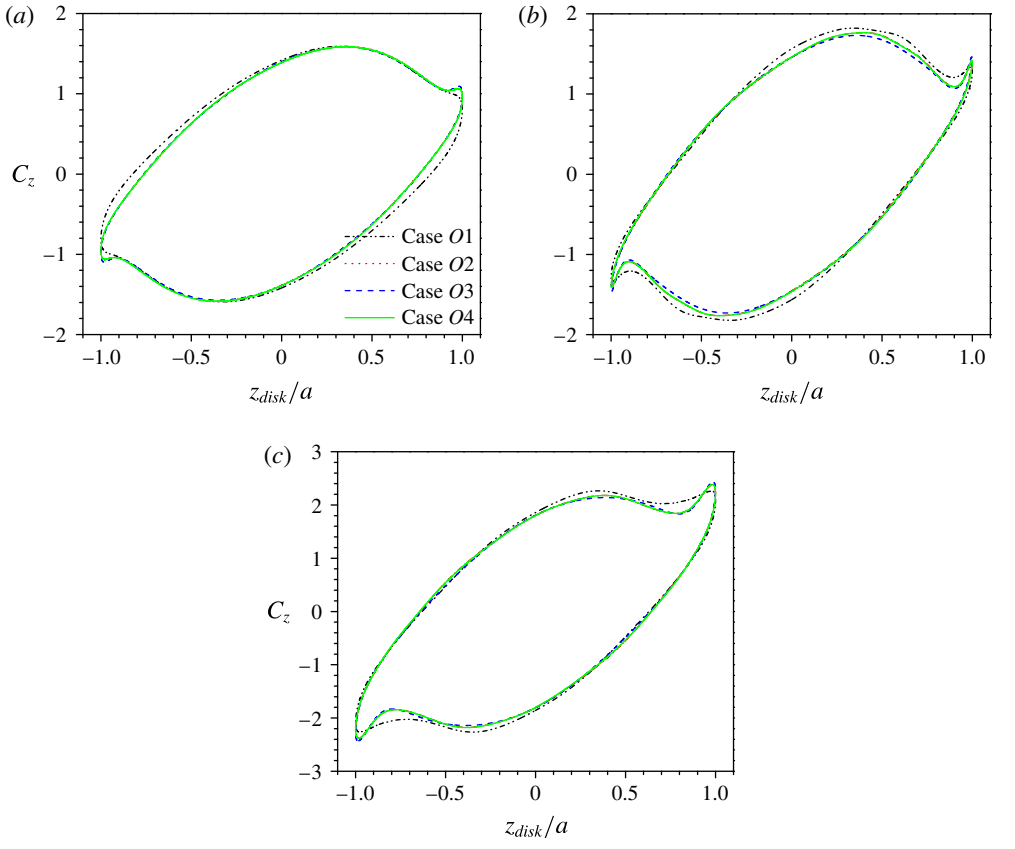


FIGURE 4. (Colour online) Axial drag coefficient (C_z) with respect to the position of the disk (z_{disk}) at (*a*) $Re = 245$ and $KC = 24.5$, (*b*) $Re = 600$ and $KC = 15$ and (*c*) $Re = 900$ and $KC = 7.5$.

C_{xy}. The details of the procedures used to determine the critical value of Re and KC corresponding to the axisymmetric and non-axisymmetric bifurcations are given in the Appendix. The two solid lines in figure 5 represent the threshold between axisymmetric and non-axisymmetric regimes. Further careful examination reveals that the non-axisymmetric flow begins to rotate around the axis of the disk as the Reynolds number increases. The boundary between the rotating and non-rotating flow regimes is identified by the dashed lines in figure 5. Finally, five flow regimes in the considered Re–KC space are revealed here: (I) axisymmetric flow (AS), (II) planar symmetric flow in the low-KC region (PSL), (III) azimuthally rotating flow in the low-KC region (ARL), (IV) planar symmetric flow in the high-KC region (PSH) and (V) azimuthally rotating flow in the high-KC region (ARH). In the following, we select one example case from each flow regime and present the corresponding force coefficients and flow visualizations.

3.1. *Regime I: axisymmetric flow (AS)*

Figure 6 shows the time traces of the force coefficients for the AS regime, where $Re = 600$ and $KC = 15$. As shown, a periodic variation in C_z is observed, indicating a well-developed flow. However, the transverse force coefficients C_x and C_y are zero.

https://doi.org/10.1017/jfm.2016.800 Published online by Cambridge University Press

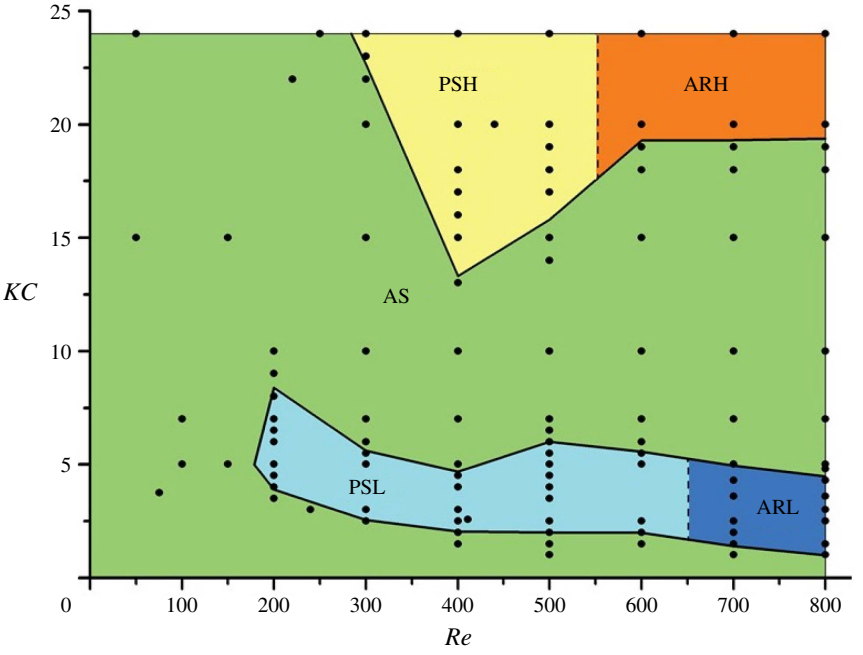


FIGURE 5. (Colour online) The critical boundaries between different flow regimes in Re–KC space.

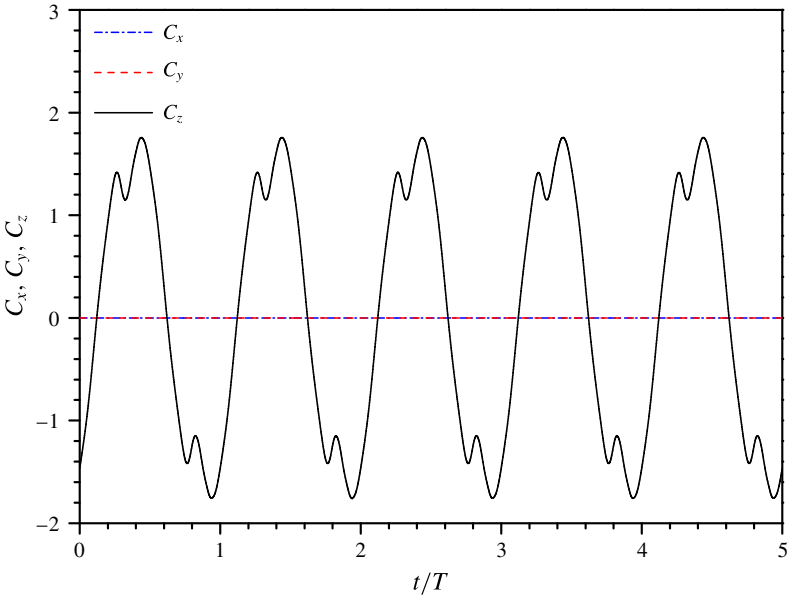


FIGURE 6. (Colour online) Time traces of the force coefficients C_x, C_y and C_z of the disk over 5 oscillation cycles in the AS regime, where $Re = 600$ and $KC = 15$.

Figure 7 shows the three-dimensional vortical structures identified based on the Q-criterion for $Re = 600$ and $KC = 15$ in the AS regime. As shown in figure 7, the

https://doi.org/10.1017/jfm.2016.800 Published online by Cambridge University Press

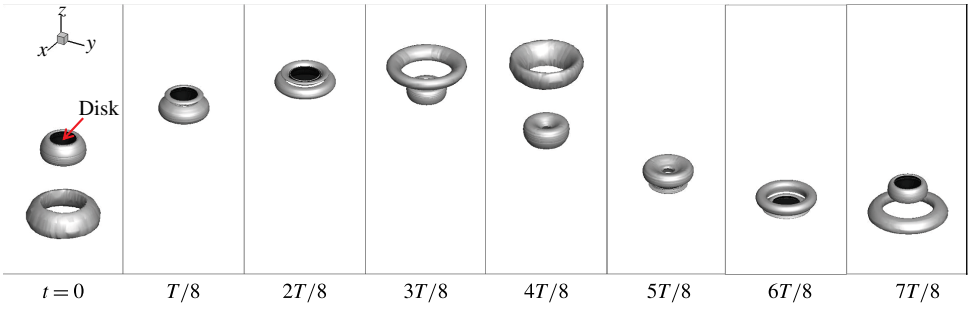


FIGURE 7. (Colour online) Vortical structures identified based on the Q-criterion during one oscillation cycle in the AS regime, where $Re = 600$ and $KC = 15$.

flow is symmetric about the axis of the disk throughout the oscillation cycle. In the presented case, circular vortex rings are repeatedly generated with the periodic oscillations of the disk (see movie 1 of the online supplementary movies available at https://doi.org/10.1017/jfm.2016.800). This vortex shedding results in oscillations in the time traces of C_z at higher frequencies. As mentioned previously, the critical Reynolds number for the non-axisymmetric bifurcation of the uniform flow normal to a circular disk with $\chi = 10$ has been reported to be $Re_{c1} \approx 135$ (Shenoy & Kleinstreuer 2008) and $Re_{c1} \approx 129.6$ (Chrust *et al.* 2010). Although the Reynolds number in the case depicted in figure 7 is 600, which is significantly higher than the reported Re_{c1} values, the flow in this oscillating case is still axisymmetric. One may argue that the Reynolds number defined for the oscillating case considered in this study is based on the maximum velocity of the disk [U_{max}, see equation (1.1)], thereby resulting in a nominally higher Reynolds number. However, if we calculate an average Reynolds number based on the average magnitude of the velocity of the oscillating disk, then this average Reynolds number is $Re_{ave} = 382$, which is still significantly higher than the reported values of Re_{c1}. This finding implies the existence of fundamental differences in fluid dynamics between a unidirectional flow and an oscillatory flow. Notably, the exactly circular vortical rings shown in figure 7 have not been observed in the wake of the uniform flow normal to a circular disk. This is because, for the uniform flow normal to a disk, the critical Reynolds number for the onset of vortex shedding is higher than the critical Reynolds number for non-axisymmetric bifurcation.

3.2. *Regime II: planar symmetric flow in the low-KC region (PSL)*

Figure 8 shows the force coefficient results for the PSL regime, where $Re = 411$ and $KC = 2.57$. As shown in figure 8(*a*), the values of C_x and C_y are comparable to the value of C_z. The time traces of the force coefficients are periodic; however, the periods of C_x and C_y are one half of the period of C_z. This finding indicates that the transverse force oscillates twice during one oscillation cycle. It is evident that the noticeable transverse force acting on the disk arises because the flow surrounding the disk is no longer axisymmetric.

The vortical structures identified based on the Q-criterion for $Re = 411$ and $KC = 2.57$ in the PSL regime are shown in figure 9. As shown in figure 9, the flow around the disk in the PSL regime appears with a planar symmetric pattern rather than with an axisymmetric pattern. As the disk oscillates, vortex shedding

https://doi.org/10.1017/jfm.2016.800 Published online by Cambridge University Press

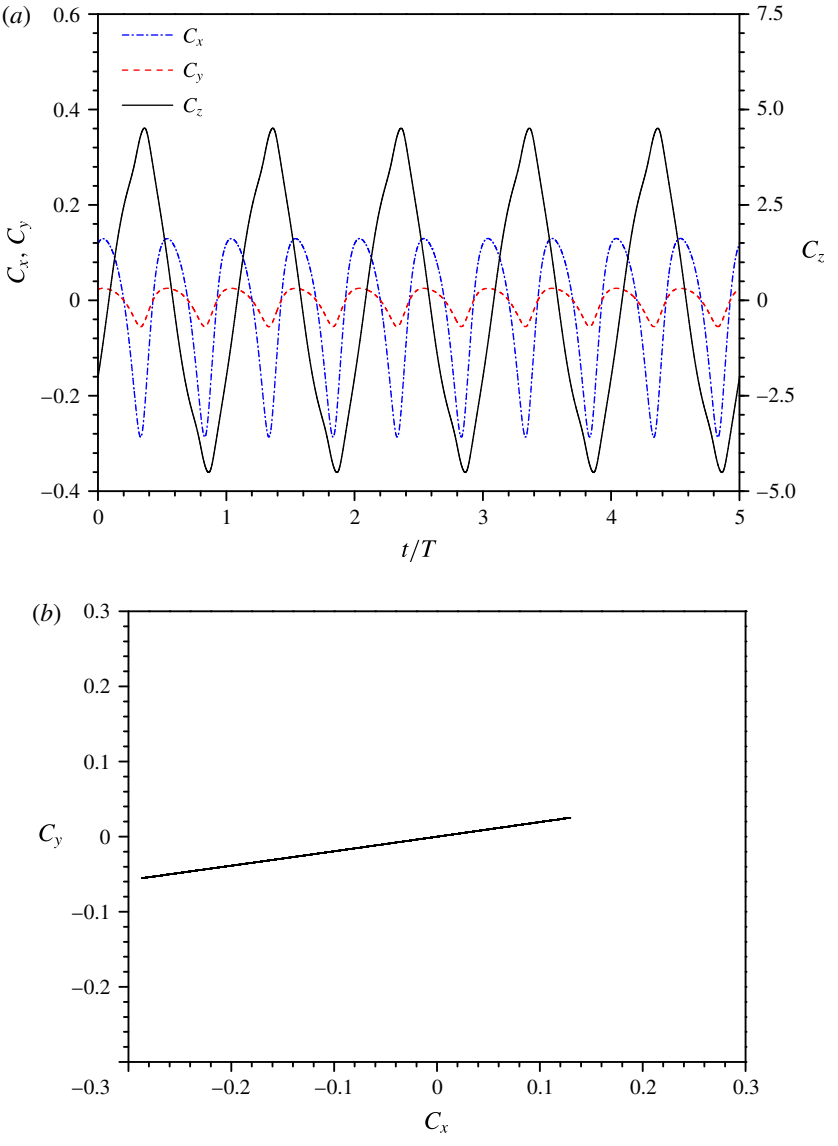


FIGURE 8. (Colour online) Force coefficient results for the disk over 5 oscillation cycles in the PSL regime, where $Re = 411$ and $KC = 2.57$: (*a*) time traces of C_x, C_y and C_z and (*b*) a phase-space plot of C_x and C_y.

initially begins along one side of the disk edge, and then, a crescent-moon-shaped vortex is generated, eventually resulting in a non-axisymmetric flow. Figure 9 shows that non-axisymmetric vortex shedding occurs twice during one oscillation cycle; accordingly, the transverse force coefficients C_x and C_y also oscillate twice in one cycle. A more detailed animation of the vortex shedding process has been included in the online supplementary material (movie 2).

Figure 8(*b*) shows the phase-space plot of the C_x and C_y time traces shown in figure 8(*a*). The transverse force acting on the disk appears to oscillate back and forth along a fixed orientation, indicating that the flow is indeed planar symmetric

https://doi.org/10.1017/jfm.2016.800 Published online by Cambridge University Press

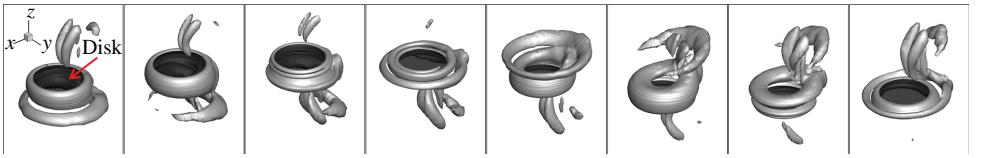


FIGURE 9. (Colour online) Vortical structures identified based on the Q-criterion during one oscillation cycle for the PSL regime, where $Re = 411$ and $KC = 2.57$.

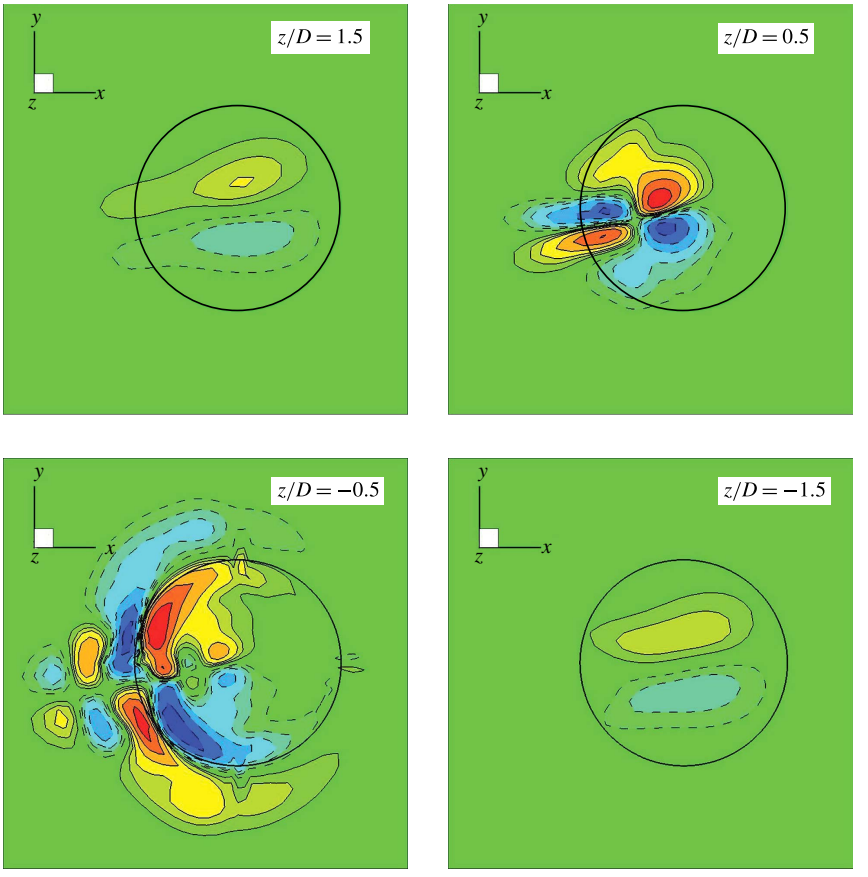


FIGURE 10. (Colour online) Contours of the axial vorticity (ω_z) on various z planes for the PSL regime, where $Re = 411$, $KC = 2.57$ and $z_{disk} = 0$. The circle is the projection of the disk. Positive and negative values of ω_z are represented by solid and dashed lines, respectively.

and that the direction of the transverse force lies within the symmetry plane. The orientation of the symmetry plane is selected randomly. As shown in figure 10, the axial vorticity (ω_z) contour plots on several z planes again demonstrate that the flow is planar symmetric. The present planar symmetric flow recalls the planar symmetric (or reflectionally symmetric) modes of the uniform flow normal to a circular disk at low Reynolds numbers, such as the SS (Fabre *et al.* 2008), 'standing wave' (SW) (Meliga

https://doi.org/10.1017/jfm.2016.800 Published online by Cambridge University Press

et al. 2009) and Zz (Auguste *et al.* 2010) modes. Notably, the planar symmetric flow is one-sided with respect to the disk axis; see the flow observations in figures 9 and 10. This is because the vortex shedding locations on the two sides of the disk are always with the same orientation; see figure 9. The resulting mean value of the transverse force acting on the disk is non-zero; see figure 8(*b*). For the uniform flow normal to a circular disk, a non-zero mean transverse force has also been observed in the SS and Zz modes.

Because a similar planar symmetric flow regime is observed in the high-*KC* region (see § 3.4), the present flow regime is referred to as the regime of planar symmetric flow in the low-*KC* region (PSL).

3.3. *Regime III: azimuthally rotating flow in the low-KC region (ARL)*

Figure 11 shows the force coefficient results for the ARL regime, where $Re = 800$ and $KC = 2.5$. Compared with the time traces of the force coefficients in the PSL regime (see figure 8*a*), the time traces of the force coefficients in the ARL regime (see figure 11*a*) are similar overall except for the slight variation in the envelopes of C_x and C_y. Figure 11(*b*) shows the phase-space plot of C_x and C_y over 64 oscillation cycles. A very slow rotation is observed in the transverse force. The arrow in figure 11(*b*) indicates the direction of rotation of the transverse force. It appears that the flow rotates slowly as the disk passes through successive oscillations. Figure 12 shows the evolution of the axial vorticity (ω_z) contour on the plane $z/D = 1$ when $z_{disk} = 0$ with a time interval of $13T$. It is observed that the flow is continuously rotating about the axis of the disk.

The vortical structures identified based on the Q-criterion for $Re = 800$ and $KC = 2.5$ in the ARL regime are shown in figure 13 and the online supplementary material (movie 3). Although the rotational motion of the flow is very slow, the three-dimensional vortical structures in the ARL regime are more complicated than those in the PSL regime; see figure 9. For the case of the flow normal to a circular disk, the flow begins to rotate about the axis of the disk after the secondary Hopf bifurcation. The planar symmetry observed in the previous SS mode no longer holds. The flow exists in a YY state instead; see figure 5 in Shenoy & Kleinstreuer (2008). However, the 'Yin-Yang' mode observed in the uniform flow normal to a circular disk is not observed in the rotating flow considered here. As shown in figure 12, the instantaneous rotating flow is approximately planar symmetric, as observed in the PSL regime; see figure 10. This implies that the planar symmetric nature of the flow in the PSL regime is inherited in the ARL regime. Therefore, similar to the flow in the PSL regime, the flow in the ARL regime is also one-sided with respect to the disk axis, and this feature is again associated with a non-zero mean transverse force (see figure 11*b*).

Because a similar azimuthal rotating flow regime is observed in the high-*KC* region (see § 3.5), the present flow regime is referred to as the regime of azimuthal rotating flow in the low-*KC* region (ARL).

3.4. *Regime IV: planar symmetric flow in the high-KC region (PSH)*

Figure 14 shows the force coefficient results for the PSH regime, where $Re = 500$ and $KC = 20$. As shown in figure 14(*a*), the values of C_x and C_y are comparable to the value of C_z, indicating a non-axisymmetric flow. Similar to the PSL regime (see figure 8*a*), the time traces of the force coefficients are periodic and the periods of C_x and C_y are one half of the period of C_z. A high-frequency fluctuation is evident in

https://doi.org/10.1017/jfm.2016.800 Published online by Cambridge University Press

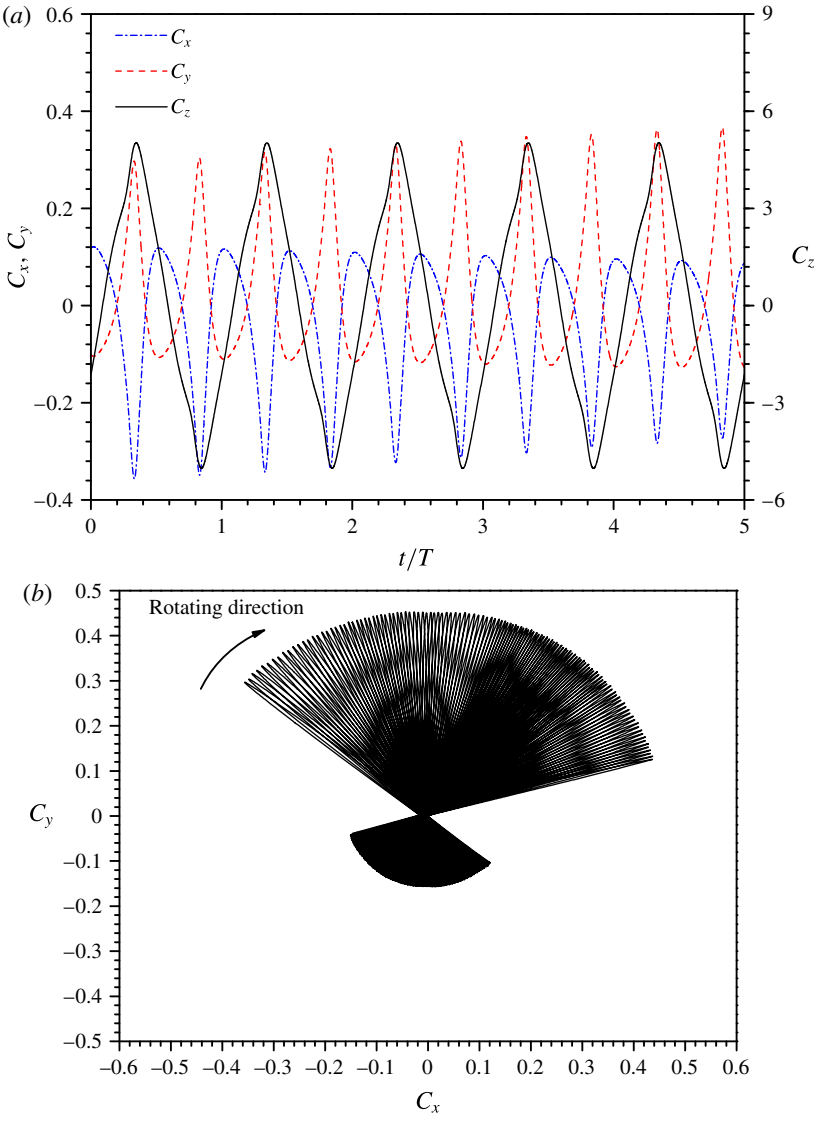


FIGURE 11. (Colour online) Force coefficient results for the disk in the ARL regime, where $Re = 800$ and $KC = 2.5$: (*a*) time traces of C_x, C_y and C_z over 5 oscillation cycles and (*b*) a phase-space plot of C_x and C_y over 64 oscillation cycles.

C_z. This is because the vortex shedding along the disk occurs more frequently in this high-KC case than that in low-KC cases.

Figure 14(*b*) shows the phase-space plot of C_x and C_y for $Re = 500$ and $KC = 20$ in the PSH regime. As observed in the PSL regime (see figure 8*b*), the transverse force acting on the disk in the PSH regime has a fixed orientation and a non-zero mean value, indicating a one-sided planar symmetric flow. The transverse force acting on the disk oscillates within the plane of symmetry.

The vortical structures identified based on the Q-criterion for the case with $Re = 500$ and $KC = 20$ in the PSH regime are shown in figure 15. For the cases at high KC,

https://doi.org/10.1017/jfm.2016.800 Published online by Cambridge University Press

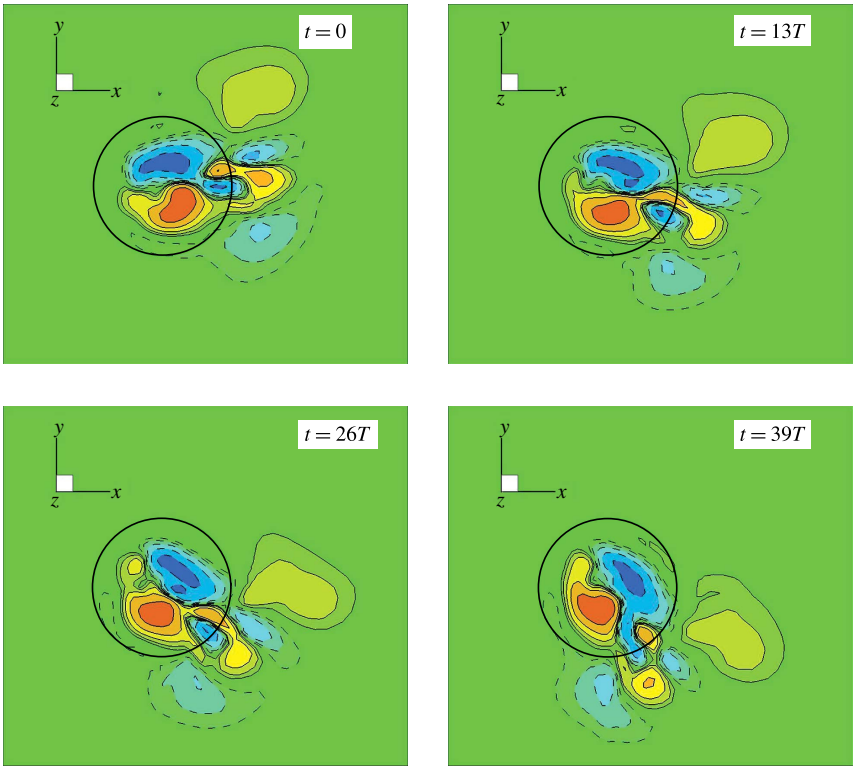


FIGURE 12. (Colour online) Evolution of the axial vorticity ω_z on the $z/D = 1$ plane for the ARL regime, where $Re = 800$, $KC = 2.5$ and $z_{disk} = 0$. The circle is the projection of the disk. Positive and negative values of ω_z are represented by solid and dashed lines, respectively.

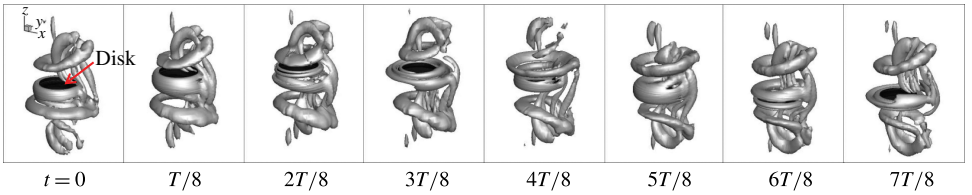


FIGURE 13. (Colour online) Vortical structures identified based on the Q-criterion during one oscillation cycle for the ARL regime, where $Re = 800$ and $KC = 2.5$.

the disk travels a farther distance and the vortical structures behind the disk are more adequately developed. Therefore, apparent hairpin vortices are observed in figure 15. However, the vortices are shed in a fixed azimuthal direction with respect to the disk, unlike the double-sided vortex shedding mode observed in the 'standing wave' (SW) mode for the flow normal to a circular disk; see figure 8 in Shenoy & Kleinstreuer (2008). Figure 16 shows the contours of the axial vorticity (ω_z) on various z planes for the case of $Re = 500$, $KC = 20$ and $z_{disk} = 0$. The findings again indicate that the flow is planar symmetric. A more detailed animation of the vortex shedding process has been included in the online supplementary material (movie 4). In consideration of

https://doi.org/10.1017/jfm.2016.800 Published online by Cambridge University Press

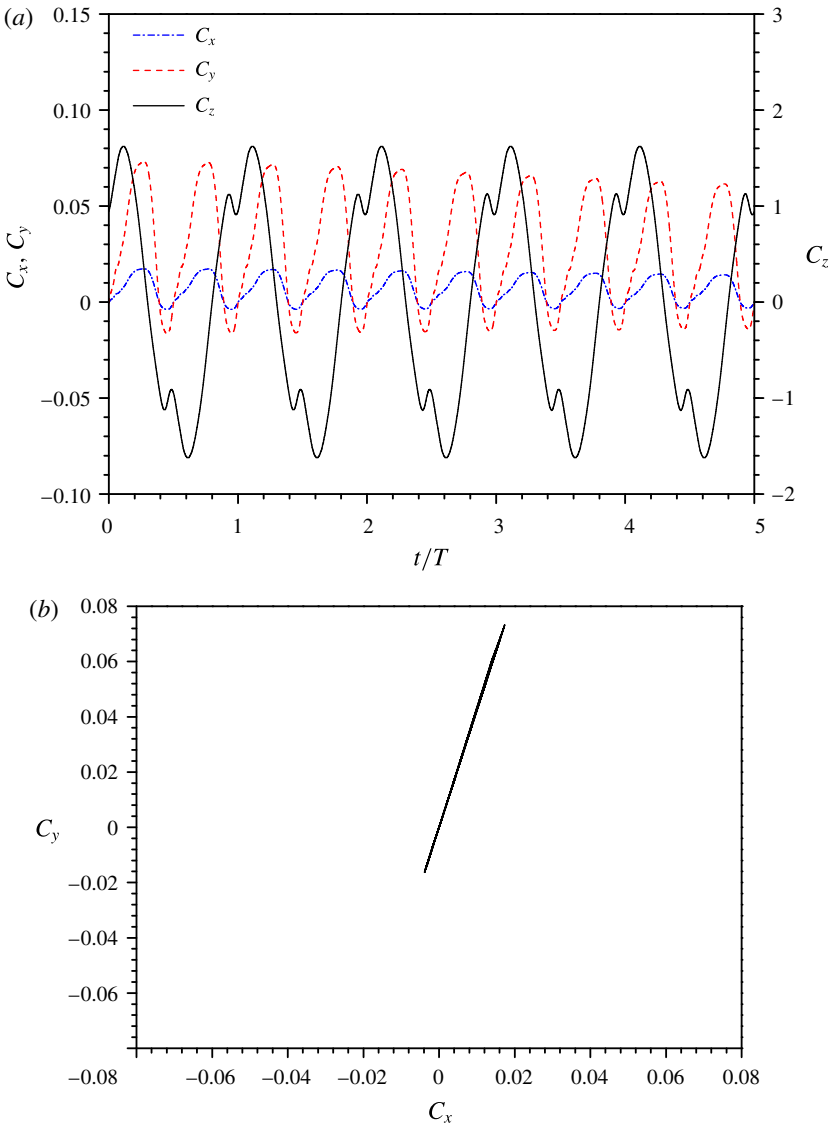


FIGURE 14. (Colour online) Force coefficient results for the disk over 5 oscillation cycles in the PSH regime, where $Re = 500$ and $KC = 20$: (*a*) time traces of C_x, C_y and C_z and (*b*) a phase-space plot of C_x and C_y.

the planar symmetric flow regime observed in the low-KC region (the PSL regime), as presented in § 3.2, the present regime is referred to as the regime of planar symmetric flow in the high-KC region (PSH).

3.5. *Regime V: azimuthally rotating flow in the high-KC region (ARH)*

Figure 17 shows the force coefficient results for the ARH regime, where $Re = 600$ and $KC = 24$. As shown in figure 17(*a*), C_z varies periodically, whereas C_x and C_y exhibit a slow variation in magnitude. The phase-space plot of C_x and C_y shown in figure 17(*b*) indicates a rotational motion of the flow. Compared with the rotational

https://doi.org/10.1017/jfm.2016.800 Published online by Cambridge University Press

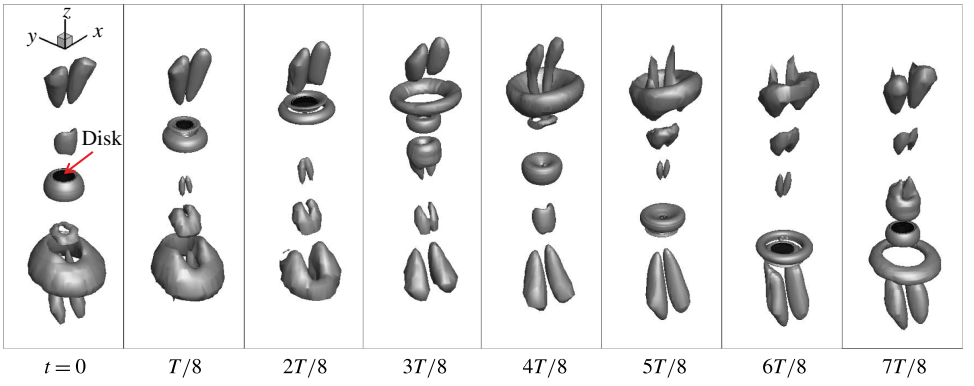


FIGURE 15. (Colour online) Vortical structures identified based on the Q-criterion during one oscillation cycle for the PSH regime, where $Re = 500$ and $KC = 20$.

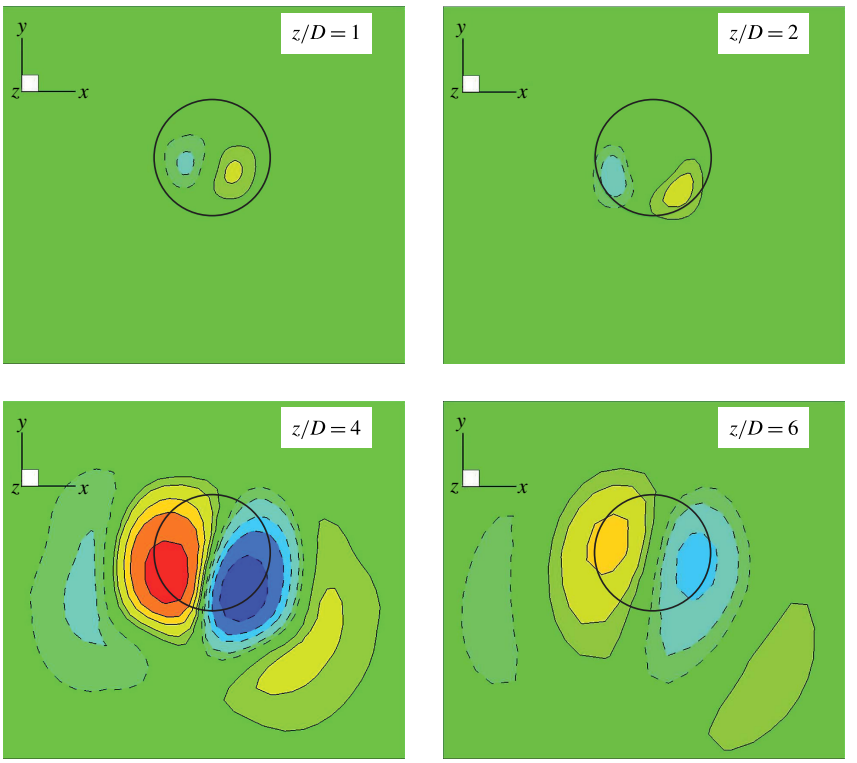


FIGURE 16. (Colour online) Contours of the axial vorticity (ω_z) on various z planes for the PSH regime, where $Re = 500$, $KC = 20$ and $z_{disk} = 0$. The circle is the projection of the disk. Positive and negative values of ω_z are represented by solid and dashed lines, respectively.

motion observed in the ARL regime (see figure 11*b*), the rotational motion seen in this case is much faster. Figure 18 shows the evolution of the axial vorticity (ω_z) contours

https://doi.org/10.1017/jfm.2016.800 Published online by Cambridge University Press

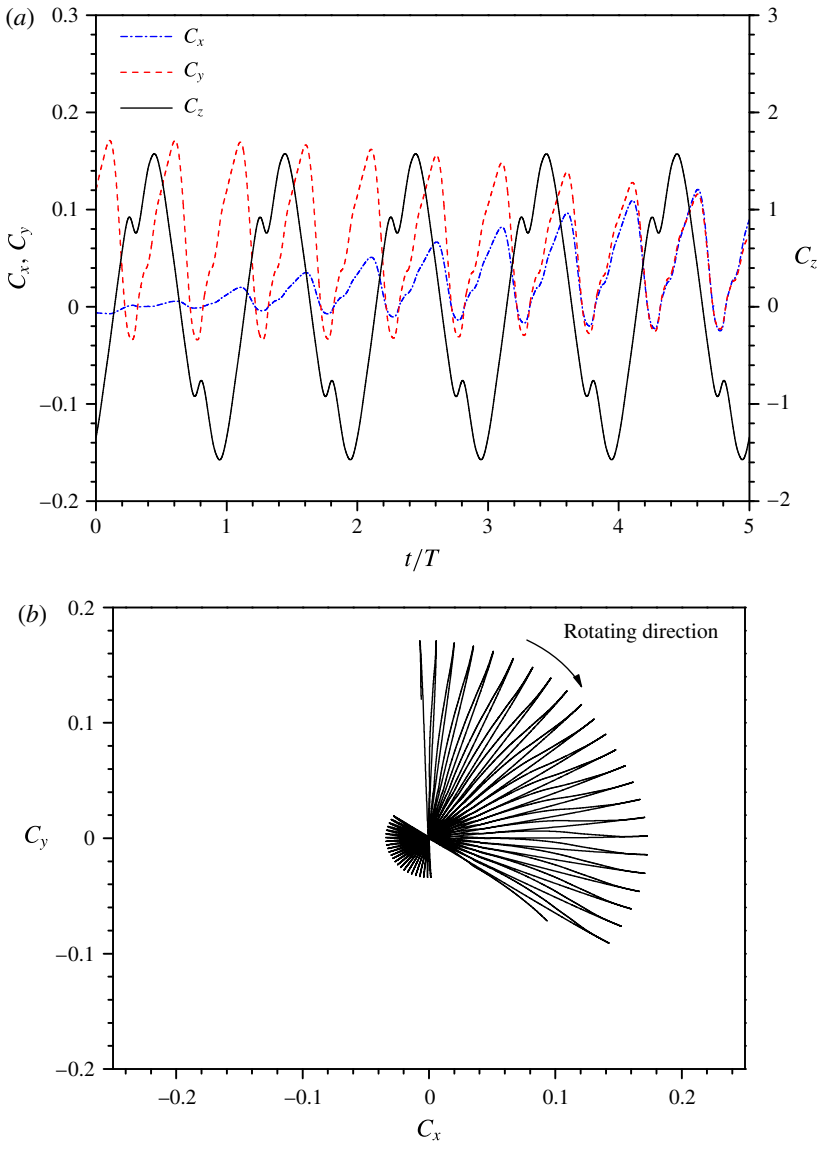


FIGURE 17. (Colour online) Force coefficient results for the disk in the ARH regime, where $Re = 600$ and $KC = 24$: (*a*) time traces of C_x, C_y and C_z over 5 oscillation cycles and (*b*) a phase-space plot of C_x and C_y over 12 oscillation cycles.

on the $z/D = 4$ plane when $z_{disk} = 0$ with a time interval of $2T$. It is observed that the flow is continuously rotating about the axis of the disk.

Figure 19 shows the variations in the vortical structures identified based on the Q-criterion during one oscillation cycle for $Re = 600$ and $KC = 24$ in the ARH regime. The observed flow structures are more disordered than those in the PSH regime; see figure 15 and the online supplementary material (movie 5). This is because the Reynolds number in the ARH regime is higher than that in the PSH regime. Hairpin vortical structures are clearly observed in figure 19, as in the wake of the uniform

https://doi.org/10.1017/jfm.2016.800 Published online by Cambridge University Press

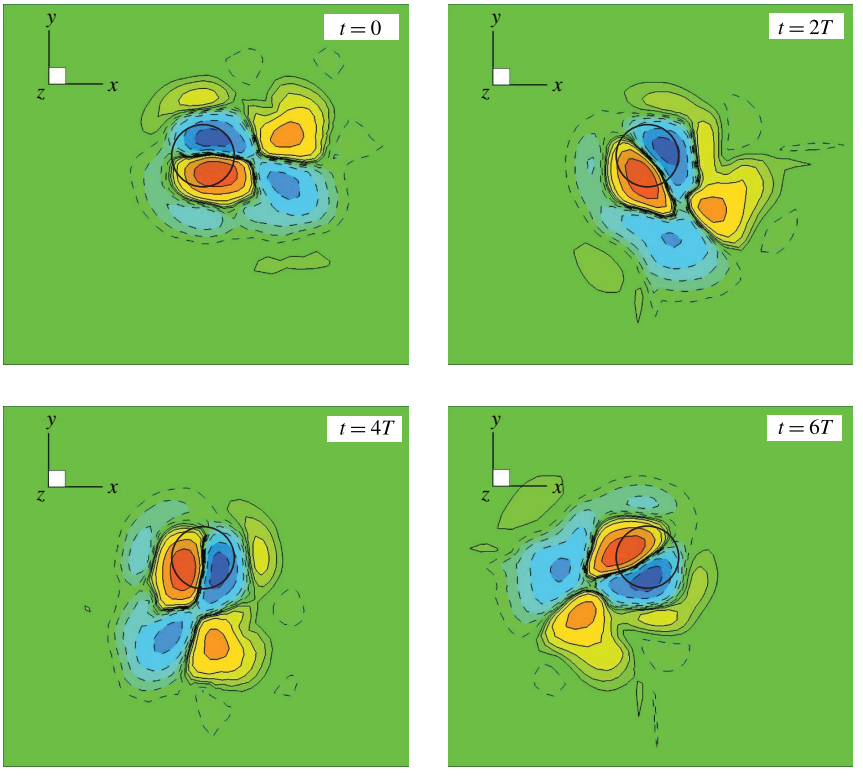


FIGURE 18. (Colour online) Evolution of the axial vorticity ω_z on the plane $z/D = 4$ for the ARH regime, where $Re = 600$, $KC = 24$ and $z_{disk} = 0$. The circle is the projection of the disk. Positive and negative values of ω_z are represented by solid and dashed lines, respectively.

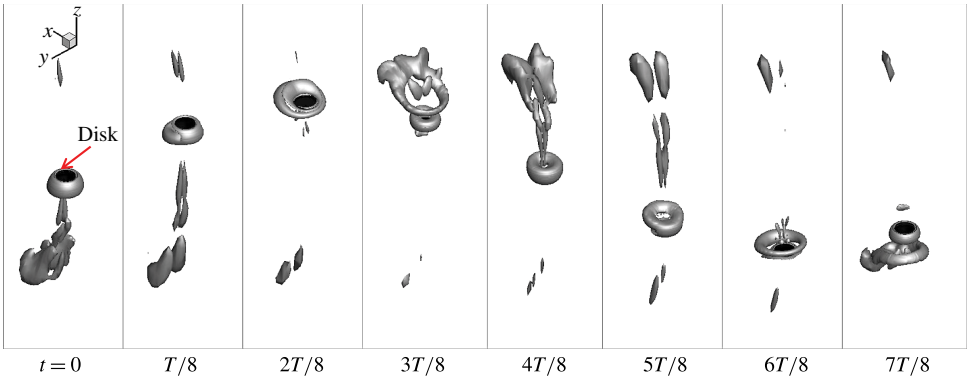


FIGURE 19. (Colour online) Vortical structures identified based on the Q-criterion during one oscillation cycle for the ARH regime, where $Re = 600$ and $KC = 24$.

flow normal to a disk. It is again observed that the vortical structures are one-sided with respect to the axis of the disk and that the mean transverse force acting on the disk is non-zero; see figure 17(*b*). In consideration of the azimuthal rotating

https://doi.org/10.1017/jfm.2016.800 Published online by Cambridge University Press

flow regime observed in the low-KC region (the ARL regime), as discussed in § 3.3, the present regime is referred to as the regime of azimuthally rotating flow in the high-KC region (ARH).

3.6. *Discussion on the steady and oscillatory flow regimes*

Recalling the bifurcation scenarios in the wake of the uniform flow normal to a thin disk (see § 1), several flow regimes are revealed successively as Re increases: 'steady axisymmetric state' (Auguste *et al.* 2010), 'steady asymmetric state' Shenoy & Kleinstreuer (2008), 'reflectional symmetry breaking' (Fabre *et al.* 2008) and later some more complicated states depending on the aspect ratio of the disk. It is noted that all these states are used for describing the 'steady- flow' situation with a constant Re. For the oscillating disk case, the 'steady-flow' situation is never held, instead, the actual Reynolds number increases and decreases as the disk oscillates. The saturated 'steady-flow' state at a particular Re is not achievable in the oscillating case. Moreover, compared with the 'steady-flow' case, the oscillating disk moves back and forth periodically, the disk may go into its own wake. However, it does not mean that the oscillating disk case is not comparable to the 'steady-flow' case. A sufficiently large KC of an oscillating disk provides a large distance for the evolution of wake flow, therefore giving us an opportunity to catch some scenario fragments which are similar to those 'steady-flow' states.

In this study, the range of KC is up to 24. At the lower part of figure 5, the regimes PSL and ARL are in the range of $2.5 < KC < 7$, approximately, corresponding to an oscillatory amplitude of $0.4D < a < 1.4D$. This amplitude is too small to have a developed wake flow, as confirmed in figures 9 and 13 and movies 2 and 3 in the online supplementary material. At the upper part of figure 5, the value of KC in the regimes PSH and ARH is up to 24, corresponding to an oscillatory amplitude of $a \approx 3.82D$. This distance allows a wake evolution as that in the 'steady-flow' case. As shown in the case of $Re = 500$ and $KC = 20$ (see figure 15), the flow is planar symmetric as described in § 3.4. At the topmost and lowest locations (see the pictures at $t = 2T/8$ and $6T/8$ respectively in figure 15), the actual instantaneous Reynolds number is very small. Therefore, the toroidal vortex is generated approximately. This could be interpreted as a co-existence of different 'steady-flow' states in the oscillating disk case, see also movie 4 in the online supplementary material. For the case of $Re = 600$ and $KC = 24$ (see figure 19), the increase in Reynolds number results in a new regime corresponding to the 'reflectional symmetry breaking state' in the 'steady-flow' case (Fabre *et al.* 2008).

It appears that there are some connections between the oscillating disk at a large KC and the 'steady-flow' case. However, it must be kept in mind that the oscillating disk case presented here are intrinsically different with the 'steady-flow' situation. In other words, the $KC = 24$ is still too small to be considered as a 'sufficiently large' KC at which those bifurcations in the 'steady-flow' case could be observed in one oscillating cycle.

4. Concluding remarks

The flow around an oscillating circular disk was investigated using the DNS approach. The disk was forced to oscillate sinusoidally along its axis. The aspect ratio (diameter/thickness) of the disk was 10. The ranges considered for the Reynolds number (Re) and the Keulegan–Carpenter number (KC) were $50 \leqslant Re \leqslant 800$ and $1 \leqslant KC \leqslant 24$, respectively. In the considered Re–KC space, one axisymmetric

https://doi.org/10.1017/jfm.2016.800 Published online by Cambridge University Press

flow regime and two non-axisymmetric flow regimes were identified. In each non-axisymmetric flow regime, the flow was planar symmetric at lower Reynolds numbers and began to rotate about the axis of the disk as the Reynolds number increased. Therefore, five flow regimes were identified: (I) axisymmetric flow (AS), (II) planar symmetric flow in the low-*KC* region (PSL), (III) azimuthally rotating flow in the low-*KC* region (ARL), (IV) planar symmetric flow in the high-*KC* region (PSH) and (V) azimuthally rotating flow in the high-*KC* region (ARH). In the non-axisymmetric flow regimes, the flow around the disk was found to be one-sided with respect to the axis of the disk and associated with a non-zero mean value of the transverse force acting on the disk.

It should be noted that the critical boundaries between the different flow regimes in the *Re*–*KC* space were determined based on a limited number of numerical simulations. More accurate boundaries could be obtained through more extensive numerical simulations. Because only one disk aspect ratio, namely, $\chi = 10$, was considered in this study, further research is planned to study the effects of the aspect ratio on the flow regimes and the critical boundaries between different flow regimes.

Acknowledgements

The authors would like to thank the support from Shanghai Yang Fan Program (grant no. 15YF1406100), the National Natural Science Foundation of China (grant nos 51509152, 11632011 and 51239007) and the Newton Research Collaboration Programme (grant no. NRCP/1415/211). The numerical simulations were supported by Center for HPC, Shanghai Jiao Tong University. The authors acknowledge the constructive comments of the reviewers which indeed improved the quality of this paper.

Supplementary movies

Supplementary movies are available at https://doi.org/10.1017/jfm.2016.800.

Appendix

This appendix provides additional information of the procedures used to determine the accurate critical *Re* and *KC* numbers for the axisymmetric and non-axisymmetric bifurcations. The threshold is determined roughly based on the extensive simulations at various *Re* and *KC* as indicated by the solid dots in figure 5. It is observed that the threshold lays between the axisymmetric case $(Re, KC) = (300, 2.5)$ and the non-axisymmetric case $(Re, KC) = (300, 3)$. Now we use a slightly perturbed flow as the initial condition for the case $(Re, KC) = (300, 3)$. As shown in figure 20(*a*), a growth of the amplitude of the transverse force coefficient C_{xy} is observed. By fitting the envelope of the time traces of C_{xy} to an exponential function of time, a growth rate of 2.2542 (see figure 20*c*) is determined (Ghidersa & Dušek 2000; Bohorquez *et al.* 2011). Similarly, the case of $(Re, KC) = (300, 2.5)$ is conducted with the solution for the case of $(Re, KC) = (300, 3)$ as an initial condition. Then, a decay of the amplitude of C_{xy} is observed and the decay rate is determined to be -0.0330 (see figure 20*b*,*d*). By linear interpolation of the amplification rates, the threshold is obtained at $(Re, KC) = (300, 2.56)$. Similar procedures are used to determine to the accurate threshold at other locations. In this study, 22 sets of simulations are performed and the determined critical *Re* and *KC* numbers are shown in table 4.

https://doi.org/10.1017/jfm.2016.800 Published online by Cambridge University Press

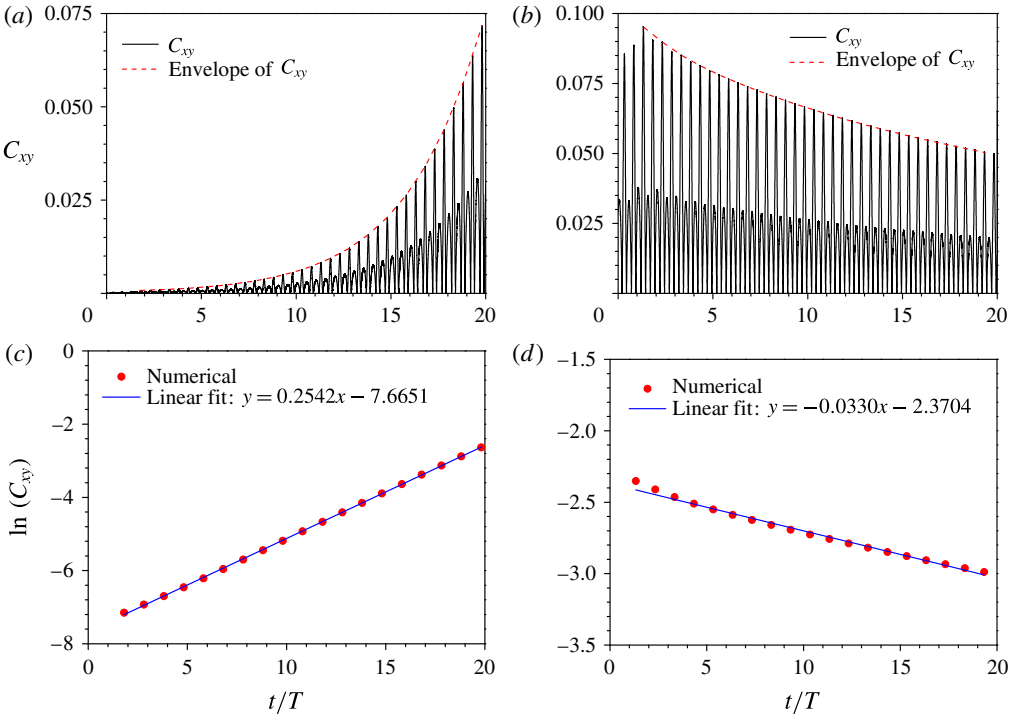


FIGURE 20. (Colour online) Determination of the growth/decay rates of the amplitude of C_{xy} for the cases based on a perturbed initial condition. The time traces of C_{xy} for the cases of (*a*) (*Re*, *KC*) = (300, 3) and (*b*) (*Re*, *KC*) = (300, 2.5), (*c*) and (*d*) the corresponding exponential fit of the envelop of C_{xy}.

(*Re*, *KC*)	(*Re*, *KC*)	(*Re*, *KC*)	(*Re*, *KC*)	(*Re*, *KC*)	(*Re*, *KC*)
(178.61, 5)	(200, 8.40)	(300, 5.63)	(400, 4.70)	(500, 6.01)	(600, 5.58)
(700, 4.96)	(800, 4.49)	(200, 3.91)	(300, 2.56)	(400, 2.07)	(500, 2.01)
(600, 1.99)	(700, 1.41)	(800, 1.00)	(300, 22.65)	(400, 13.3)	(500, 15.79)
(600, 19.28)	(700, 19.29)	(800, 19.37)	(284.12, 24)		

TABLE 4. Critical *Re* and *KC* numbers for the axisymmetric and non-axisymmetric bifurcations.

REFERENCES

AN, H., CHENG, L. & ZHAO, M. 2011 Direct numerical simulation of oscillatory flow around a circular cylinder at low Keulegan–Carpenter number. *J. Fluid Mech.* **666**, 77–103.

AUGUSTE, F., FABRE, D. & MAGNAUDET, J. 2010 Bifurcations in the wake of a thick circular disk. *Theor. Comput. Fluid Dyn.* **24** (1), 305–313.

AUGUSTE, F., MAGNAUDET, J. & FABRE, D. 2013 Falling styles of disks. *J. Fluid Mech.* **719**, 388–405.

BEARMAN, P. W. 1984 Vortex shedding from oscillating bluff bodies. *Annu. Rev. Fluid Mech.* **16** (1), 195–222.

BERGER, E., SCHOLZ, D. & SCHUMM, M. 1990 Coherent vortex structures in the wake of a sphere and a circular disk at rest and under forced vibrations. *J. Fluids Struct.* **4** (3), 231–257.

https://doi.org/10.1017/jfm.2016.800 Published online by Cambridge University Press

BOHORQUEZ, P., SANMIGUEL-ROJAS, E., SEVILIA, A., JIMÉNEZ-GONZÁLEZ, J. I. & MARTÍNEZ-BAZÁN, C. 2011 Stability and dynamics of the laminar wake past a slender blunt-based axisymmetric body. *J. Fluid Mech.* **676**, 110–144.

CHRUST, M., BOUCHET, G. & DUŠEK, J. 2010 Parametric study of the transition in the wake of oblate spheroids and flat cylinders. *J. Fluid Mech.* **665**, 199–208.

CHRUST, M., BOUCHET, G. & DUŠEK, J. 2014 Effect of solid body degrees of freedom on the path instabilities of freely falling or rising flat cylinders. *J. Fluids Struct.* **47**, 55–70.

CHRUST, M., DAUTEUILLE, C., BOBINSKI, T., ROKICKI, J., GOUJON-DURAND, S., WESFREID, J. E., BOUCHET, G. & DUŠEK, J. 2015 Effect of inclination on the transition scenario in the wake of fixed disks and flat cylinders. *J. Fluid Mech.* **770**, 189–209.

ERN, P., RISSO, F., FABRE, D. & MAGNAUDET, J. 2012 Wake-induced oscillatory paths of bodies freely rising or falling in fluids. *Annu. Rev. Fluid Mech.* **44**, 97–121.

FABRE, D., AUGUSTE, F. & MAGNAUDET, J. 2008 Bifurcations and symmetry breaking in the wake of axisymmetric bodies. *Phys. Fluids* **20**, 051702.

FERNANDES, P. C., RISSO, F., ERN, P. & MAGNAUDET, J. 2007 Oscillatory motion and wake instability of freely rising axisymmetric bodies. *J. Fluid Mech.* **573**, 479–502.

GHIDERSA, B. & DUŠEK, J. 2000 Breaking of axisymmetry and onset of unsteadiness in the wake of a sphere. *J. Fluid Mech.* **423**, 33–69.

HUNT, J. C. R., WRAY, A. A. & MOIN, P. 1988 Eddies, streams, and convergence zones in turbulent flows. In *Center for Turbulence Research Report CTR-S88*, pp. 193–208. NASA.

KUO, Y. H. & BALDWIN, L. V. 1967 The formation of elliptical wakes. *J. Fluid Mech.* **27** (02), 353–360.

MARSHALL, D. & STANTON, T. E. 1931 On the eddy system in the wake of flat circular plates in three dimensional flow. *Proc. R. Soc. Lond.* A **130** (813), 295–301.

MELIGA, P., CHOMAZ, J. M. & SIPP, D. 2009 Global mode interaction and pattern selection in the wake of a disk: a weakly nonlinear expansion. *J. Fluid Mech.* **633**, 159–189.

MICHAEL, P. 1966 Steady motion of a disk in a viscous fluid. *Phys. Fluids* **9**, 466–471.

MORISON, J. R., O'BRIEN, M. P., JOHNSON, J. W. & SCHAAF, S. A. 1950 The force exerted by surface waves on piles. *Petrol. Trans. AIME* **189**, 149–157.

NATARAJAN, R. & ACRIVOS, A. 1993 The instability of the steady flow past spheres and disks. *J. Fluid Mech.* **254**, 323–344.

OPENFOAM 2009 *The Open Source CFD Toolbox, Programmer's Guide, Version 1.6*. OpenCFD Limited.

RIMON, Y. 1969 Numerical solution of the incompressible time-dependent viscous flow past a thin oblate spheroid. *Phys. Fluids* **12**, II–65–75.

RIVET, J. P., HENON, M., FRISCH, U. & D'HUMIERES, D. 1988 Simulating fully three-dimensional external flow by lattice gas methods. *Europhys. Lett.* **7**, 231.

ROBERTS, J. B. 1973 Coherence measurements in an axisymmetric wake. *AIAA J.* **11**, 1569–1571.

ROOS, F. W. & WILLMARTH, W. W. 1971 Some experimental results on sphere and disk drag. *AIAA J.* **9**, 285–291.

SHENOY, A. R. & KLEINSTREUER, C. 2008 Flow over a thin circular disk at low to moderate Reynolds numbers. *J. Fluid Mech.* **605**, 253–262.

SHENOY, A. R. & KLEINSTREUER, C. 2010 Influence of aspect ratio on the dynamics of a freely moving circular disk. *J. Fluid Mech.* **653**, 463–487.

TCHOUFAG, J., FABRE, D. & MAGNAUDET, J. 2014 Global linear stability analysis of the wake and path of buoyancy-driven disks and thin cylinders. *J. Fluid Mech.* **740**, 278–311.

WELLER, H. G., TABOR, G., JASAK, H. & FUREBY, C. 1998 A tensorial approach to computational continuum mechanics using object-oriented techniques. *Comput. Phys.* **12**, 620–631.

WILLIAMSON, C. H. K. & GOVARDHAN, R. 2008 A brief review of recent results in vortex-induced vibrations. *J. Wind Engng Ind. Aerodyn.* **96**, 713–735.

WILLMARTH, W. W., HAWK, N. E. & HARVEY, R. L. 1964 Steady and unsteady motions and wakes of freely falling disks. *Phys. Fluids* **7**, 197–208.

YANG, J., LIU, M., WU, G., LIU, Q. & ZHANG, X. 2015 Low-frequency characteristics in the wake of a circular disk. *Phys. Fluids* **27** (6), 064101.

https://doi.org/10.1017/jfm.2016.800 Published online by Cambridge University Press

YANG, J., LIU, M., WU, G., ZHONG, W. & ZHANG, X. 2014*a* Numerical study on coherent structure behind a circular disk. *J. Fluids Struct.* **51**, 172–188.

YANG, J., TIAN, X. & LI, X. 2014*b* Hydrodynamic characteristics of an oscillating circular disk under steady in-plane current conditions. *Ocean Engng* **75**, 53–63.

YANG, J., WU, G., ZHONG, W. & LIU, M. 2014*c* Numerical study on bifurcations in the wake of a circular disk. *Intl J. Comput. Fluid Dyn.* **28** (5), 187–203.

ZHONG, H. J. & LEE, C. B. 2012 The wake of falling disks at low Reynolds numbers. *Acta Mechanica Sin.* **28**, 1–5.

https://doi.org/10.1017/jfm.2016.800 Published online by Cambridge University Press